Finding realistic dike models from interferometric synthetic aperture radar data: The February 2000 eruption at Piton de la Fournaise

Y. Fukushima, Valérie Cayol, P Durand

Finding realistic dike models from interferometric synthetic aperture radar data: The February 2000 eruption at Piton de la Fournaise

Y. Fukushima and V. Cayol
Laboratoire Magmas et Volcans, Université Blaise Pascal, CNRS UMR 6524, Clermont-Ferrand, France

P. Durand
Centre National d'Etudes Spatiales, Toulouse, France

Received 28 June 2004; revised 2 December 2004; accepted 3 January 2005; published 23 March 2005.

[1] Dike intrusions often cause complex ground displacements that are not sufficiently explained by simple analytical models. We develop a method to find complex and realistic dike geometries and overpressures from interferometric synthetic aperture radar (InSAR) data. This method is based on a combination of a boundary element method with realistic topography and a neighborhood algorithm inversion. Dike model geometry is roughly a quadrangle with its top reaching the ground. The inversion has two stages: search and appraisal. The appraisal stage involves calculations of model marginal probability density functions using misfit values calculated during the search stage. The misfit function takes into account the variance and correlation of data noise. Synthetic tests show that a model is successfully retrieved within predicted narrow confidence intervals. We apply the method on InSAR data of the February 2000 flank eruption at Piton de la Fournaise and get a trapezoid dike dipping seaward (61.0°–67.3°) with its bottom passing 800–1000 m beneath the summit. A model with a basal slip plane does not better explain observed asymmetric displacements, and thus this asymmetry is solely attributed to the dipping dike. The dike lies above a narrow band of preeruption seismicity, suggesting that lateral magma propagation occurred. Neglecting topography results in poor modeling at depth and in overestimations of overpressure (or opening), height (both about 30%), and volume (about 20%).

Citation: Fukushima, Y., V. Cayol, and P. Durand (2005), Finding realistic dike models from interferometric synthetic aperture radar data: The February 2000 eruption at Piton de la Fournaise, *J. Geophys. Res.*, *110*, B03206, doi:10.1029/2004JB003268.

1. Introduction

[2] In the domain of ground deformation modeling, analytical solutions have frequently been used [e.g., *Mogi*, 1958; *Okada*, 1985]. There are mainly three reasons for this: (1) the calculations are simple and rapid, (2) observations were in some cases sufficiently explained by the models, and (3) the quality and quantity of deformation data were not enough to consider more complex models. The second and third reasons are linked; indeed, we can only evaluate models within the resolution and precision of data. Interferometric synthetic aperture radar (InSAR) data measure high-resolution and large-scale ground displacements [*Massonnet and Feigl*, 1998]. InSAR data often indicate complex displacements that cannot be sufficiently explained by simple analytical models.

[3] On the other hand, numerical modeling methods offer more complex and realistic analyses. For example, a three-dimensional mixed boundary element method (BEM) for linear elastic media [*Cayol and Cornet*, 1997, 1998] can incorporate realistic topography and any number of pressure sources and/or shear faults of arbitrary shape. The main disadvantage of numerical modeling in inversion problems is long calculation time. Previous studies only applied inversions with limited iterations [*Beauducel and Cornet*, 1999] or restricted its use to overpressure or slip estimation on a fixed source geometry [*Cervelli et al.*, 2002; *Masterlark*, 2003]. However, advances in computer performance and modeling techniques are making detailed inversions practicable.

[4] The method presented here aims to extract more complex and realistic dike models from InSAR data than simple rectangular dikes assumed by most previous studies. The mixed BEM is used to compute the ground displacements. The neighborhood algorithm [*Sambridge*, 1999a], one of the Monte Carlo inversion methods, is used to search for good data-fitting dike models. Each forward modeling involves a remeshing of the dike and a boundary element computation. Once the search converges, the models evaluated during the search process are used to estimate the model confidence intervals and trade-offs [*Sambridge*, 1999b]. This model appraisal is done by constructing the posterior probability density function (PPD), which is, by

0148-0227/05/2004JB003268$09.00

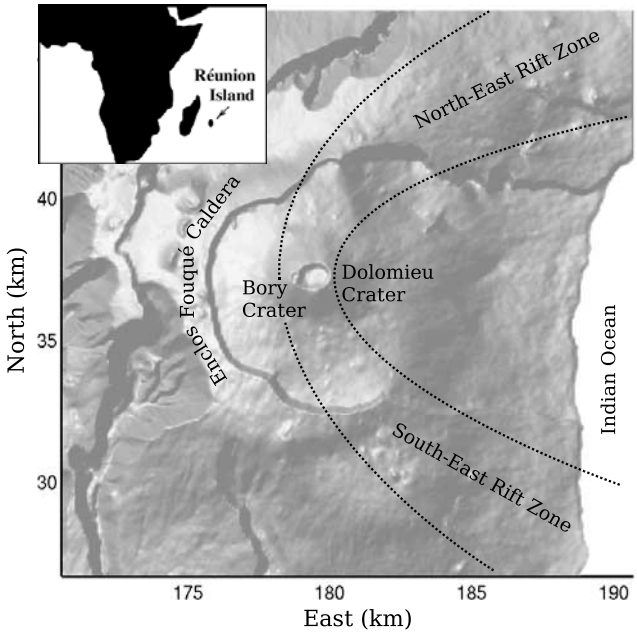

Figure 1. Geographical setting of Piton de la Fournaise. The volcano has two summit craters, Bory and Dolomieu, and a horseshoe-shaped depression called Enclos Fouqué caldera. The coordinates are given in Gauss-Laborde kilometric coordinates.

definition, the solution to an inverse problem from the Bayesian viewpoint. The appraisal stage involves no forward modeling, contrary to the procedures normally taken in Monte Carlo inversions [e.g., *Cervelli et al.*, 2001; *Wright et al.*, 2003].

[5] The developed method is tested with synthetic data, in order to find appropriate inversion settings and to check the method capabilities. It is then applied to the dike intrusion associated with the February 2000 eruption at Piton de la Fournaise volcano (Figure 1). The displacements caused by this dike intrusion were captured by the Canadian RADARSAT-1 satellite from two ascending and two descending orbits. This rich data set is suitable for testing and evaluating the developed method.

2. Method

2.1. Modeling: Mixed BEM

[6] The mixed BEM is based on a combination of two boundary element methods: the direct method and displacement discontinuity method. The direct method allows accurate and fast modeling of structures such as topography, cavities or reservoirs, whereas the displacement discontinuity method is suitable for fractures. The edifice is assumed to be linearly elastic, homogeneous and isotropic. The prescribed boundary conditions are tractions; they represent perturbations of an initial state of stress, and are null on the ground and equal to overpressure on deformation sources. Precision of the mixed BEM has been carefully tested [*Cayol and Cornet*, 1997] and the method has been applied to several studies [e.g., *Beauducel and Cornet*, 1999; *Cayol et al.*, 2000; *Dieterich et al.*, 2000].

2.1.1. Boundary Meshing

[7] Structures (in our case, the ground surface and a dike) are meshed by planar triangle elements. The ground mesh used in this study (Figure 2) is made from a digital elevation model (DEM). The mesh size is chosen in such a way that the edge effect can be neglected; we use a mesh covering a circular area of 6 km in radius. This area is about 5 times as large as the presumed deformation source dimension. The mesh is denser close to the eruptive fissures (bold lines in Figure 2) where displacement gradients are large, and coarser farther away. The caldera boundary is not explicitly considered because the data show no displacement continuity across the caldera wall. A dike mesh is generated automatically before each forward boundary element computation. Its geometry is determined by six model parameters that will be defined later.

[8] Model computation time is proportional to the square of the number of calculation points when disk swap is not required. We seek mesh densities that minimize computation time without significant loss of precision. Precision is evaluated by the following two error functions. The first one is

$$\mathrm{Err}(\%) = \frac{\sum |u_{\mathrm{ref}} - u|}{\sum |u_{\mathrm{ref}}|} \times 100, \tag{1}$$

which compares displacements on a coarse mesh u with the reference displacements on a fine mesh u_{ref}. The second one is

$$\mathrm{Err}_{\mathrm{rel}}(\%) = \frac{\sum |u_{\mathrm{ref}} - ku|}{\sum |u_{\mathrm{ref}}|} \times 100, \tag{2}$$

where a constant k is determined analytically to minimize the function. This second function evaluates the differences only in displacement patterns. As ground mesh nodes are

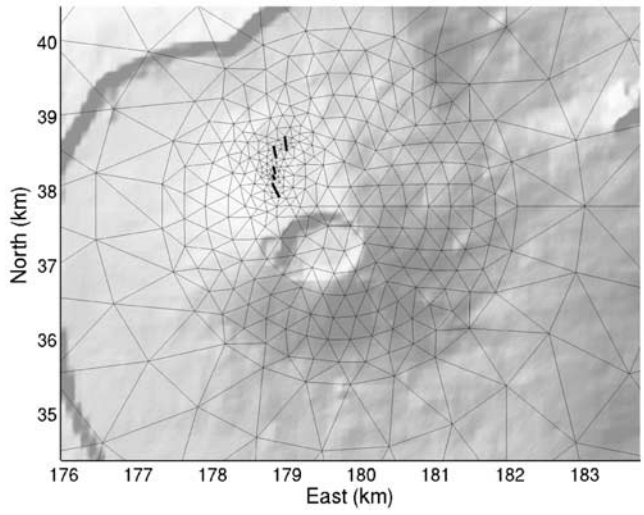

Figure 2. Part of the ground mesh used in this study superposed on a shaded relief map. The mesh includes eruptive fissure lines (bold line) which are shared by the dike mesh.

Table 1. Calculation Time and Precision for Different Mesh Intervals

Average Interval, m	Calculation Time, s	Err, %	Err_{rel}, %	k
30[a]	332			
90	30	9.8	0.98	0.91
150	20	15.3	1.80	0.87
300	15	29.1	3.60	0.78

[a]Reference mesh.

heterogeneously distributed, computed displacements are interpolated within a 100 m spacing uniform grid covering significantly displaced area to evaluate the errors.

[9] For a ground mesh with 376 elements, we obtain a negligible displacement error with Err 2.4%, where the reference displacements are computed using a very dense mesh (1286 elements). For dikes, we test three mesh densities with average node intervals of 90, 150, and 300 m, where the reference mesh assumes 30 m. Table 1 shows that relative displacement errors Err_{rel} are 1 order less than displacement errors Err. It suggests that displacements with acceptable precision can be obtained by multiplying the displacements computed using a coarse dike mesh by the scaling factor k. We observe that k is smaller than unity for all the cases, which indicates that displacements are overestimated. This seems to be a general effect of discretization in the displacement discontinuity method [*Crouch and Starfield*, 1983]. In the framework of linear elasticity, displacements are proportional to the imposed overpressure. Thus, using a coarse mesh only results in overpressure underestimation by a factor of k. By taking into account the calculation time and Err_{rel}, we consider that dike mesh density with 150 m of node interval is most appropriate to our problem. Overpressure values are rescaled once a search run is finished (section 4.3.1).

2.1.2. Model Parameters

[10] We assume that the directions of the en echelon eruptive fissures are due to rotation of the maximum principal stress close to the ground and that these fissures are linked to a single dike at depth. Under this assumption, we model a dike with two parts: a superficial part and a deeper part (Figure 3).

[11] The superficial part is made of several segments; their top is connected to the ground at the locations of the eruptive fissures, and their bottom is connected to the deeper part. The deeper part is roughly a quadrangle. Its top is a smooth curve that runs 100 m below the surface fissures. We verified that varying this depth in the range 0–200 m has a negligible influence on our problem. The bottom of the quadrangle is a straight line whose position and geometry are determined by six parameters (Figure 4). These parameters are chosen in order to be able to restrict the search to mechanically plausible dike geometries. Three parameters, i.e., dip angle (Dip), angle between the line that connects the middle points of the top and bottom sides and the direction of the maximum gradient (Shear) and elevation of the bottom middle point (Botelv), determine the position of the bottom middle point. The other three parameters, i.e., length of the bottom side scaled by that of the top side (Botlen), horizontal angle between the top and bottom sides (Twist) and vertical angle of the bottom side (Botang), determine the position of the two end points of the bottom side. We use constant overpressure (P_0) as another model parameter, which makes a total of seven model parameters.

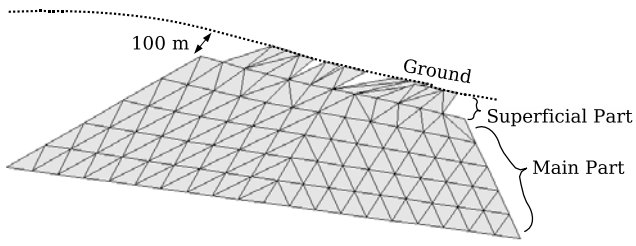

Figure 3. Example of a dike mesh. It consists of a superficial part and a deeper part. Each segment of the superficial part reaches an eruptive fissure on the ground surface and is connected to the deeper part. The deeper part is roughly a quadrangle whose geometry can change while its top side is fixed to the superficial part at 100 m from the ground.

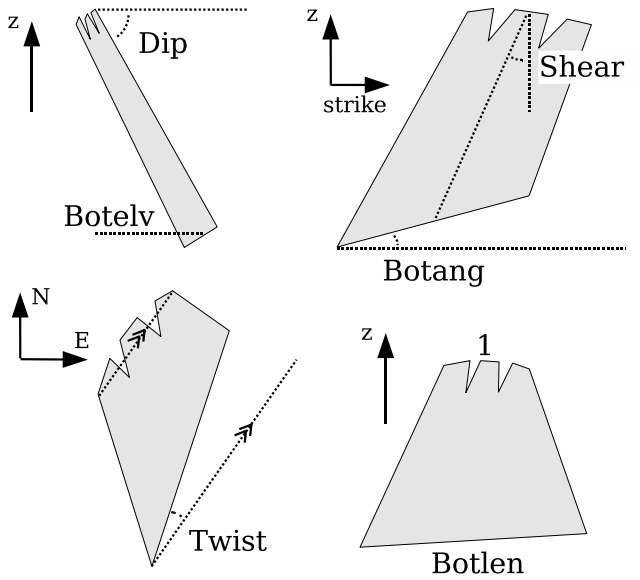

Figure 4. Six parameters used to determine the dike model geometry. These parameters were chosen to be able to restrict the geometry to physically plausible models. See text for explanations of the parameters.

2.1.3. Elastic Moduli

[12] Deformations in linearly elastic, homogeneous and isotropic media are controlled by two elastic moduli. We use Young's modulus E and Poisson's ratio ν. Displacement amplitudes are proportional to Young's modulus. We use E = 5 GPa, which was estimated by *Cayol and Cornet* [1998] for Piton de la Fournaise from in situ density [*Rançon et al.*, 1989] and seismic velocities [*Nercessian et al.*, 1996] with correction to a static value. As for Poisson's ratio, we evaluate its effect using the error function (equation (1)) in the range 0.1–0.4. The maximum error found is Err = 4.0%, with ν = 0.25 assumed as the reference. This error is much smaller than what we obtain by changing the model parameter values in a realistic range, suggesting that fixing this modulus will

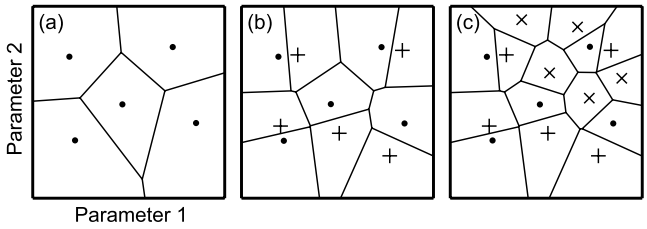

Figure 5. Example showing the search process, in the case $n = 5$ in two model dimensions. (a) Initial. Five initial models (dots) are randomly generated, and Voronoi cells are defined. (b) First iteration. Five new models (pluses) are generated in the Voronoi cells around the five best models (in this case, in every initial cell), and new Voronoi cells are defined. (c) Second iteration. Five new models (crosses) are generated around the five best models, and new Voronoi cells are defined. Note that the newly generated points modify the shapes of the surrounding cells.

little affect the estimation of the model parameters. We use $\nu = 0.25$ for our calculations.

2.2. Model Space Search

[13] In order to find the models that well explain observed data, a misfit function is defined to quantify the discrepancy between observed and modeled data. An inversion algorithm then searches for a model that minimizes the misfit within the predefined model parameter bounds.

2.2.1. Neighborhood Algorithm

[14] The neighborhood search algorithm [*Sambridge*, 1999a] aims to preferentially search good data-fitting (low misfit) regions in the model space, rather than find a single optimal model. It has already been used in some studies on ground deformation modeling. *Lohman et al.* [2002] applied this algorithm to estimate the location and slip of an earthquake fault from InSAR data and seismic waveforms. *Pritchard and Simons* [2002] used it to estimate the locations and volume changes of volcanic pressure sources from InSAR data.

[15] The algorithm we use works as follows (Figure 5). First, n initial models are randomly chosen. This is equivalent to generating n random points in the model space. Misfits at the n points are then calculated. Next, at each iteration, n points are newly generated in the neighborhood of the n lowest misfit points (one point in each), and misfits for the new points are calculated. Iterations continue until the misfit is not significantly lowered any more. The neighborhood around a point is defined by a Voronoi cell, which covers the region closer to that point than any other point (see Figure 5). Small n leads to a concentrated search in a limited model region and quick convergence, while large n leads to extensive search and slow convergence. The original method allows more complex algorithms (see *Sambridge* [1999a] for details).

[16] We use a misfit function expressed as

$$\chi^2(\mathbf{m}) = (\mathbf{u}_o - \mathbf{u}_m)^T C_d^{-1} (\mathbf{u}_o - \mathbf{u}_m), \tag{3}$$

where $\mathbf{u}_o$ and $\mathbf{u}_m$ represent observed and modeled displacements, respectively. The data covariance matrix C_d accounts for the uncertainties of observed displacements and their correlations. It is determined from InSAR noise analysis as explained later in this section.

[17] For convenience, we define a maximum misfit $\chi^2_{\max}$,

$$\chi^2_{\max} = \mathbf{u}_o^T C_d^{-1} \mathbf{u}_o. \tag{4}$$

A misfit is replaced by $\chi^2_{\max}$ in the following two cases: (1) it is greater than $\chi^2_{\max}$, (2) the dike intersects the ground. The search stops when the standard deviation of the n misfit values in one iteration becomes less than 0.3% of $\chi^2_{\max}$. This threshold was empirically determined and hence it is not applicable to other problems.

2.2.2. Data Covariance Matrix

[18] SAR interferograms have correlated noise caused by atmospheric disturbances. Correlated random noise is expressed by the autocorrelation function or covariance function [e.g., *Tarantola*, 1987]. Specifically, the exponential autocorrelation function is expressed as

$$C(r) = \sigma_d^2 \exp(-r/a), \tag{5}$$

where r is the spatial lag, σ_d^2 is the variance of the noise, and a is the correlation length. This equation indicates that noise of two data points between which the distance is over the correlation distance a is practically uncorrelated.

[19] We calculate the autocorrelation function of InSAR data noise by assuming its randomness. We follow the procedure described by *Fukushima et al.* [2003], who calculated the autocorrelations of velocity fluctuations in rocks samples. The autocorrelation function may depend on the size of the calculation area. We are not interested in the correlations of wavelengths longer than the maximum distance between points, thus the autocorrelation is calculated for spatial lags smaller than the size of the area used in the inversions. Figure 6a shows the autocorrelation

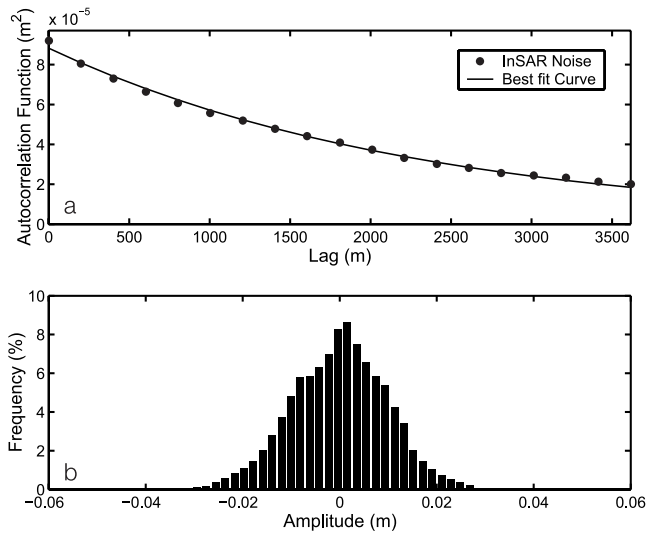

Figure 6. (a) Autocorrelation function estimated from the noise part of the four InSAR data sets (dots) and the best fit exponential curve (solid curve). The good fit indicates that the exponential autocorrelation function well represents the noise characteristics. (b) Histogram of the noise amplitudes. It is consistent with a Gaussian distribution.

function averaged over our four InSAR data sets plotted against spatial lag. The calculation was made in a roughly circular area of 7 km in diameter, with the area affected by the eruption masked. The InSAR noise is well approximated by the exponential-type random noise. The estimated variance σ_d^2 and correlation length a from the fitting are 8.8×10^{-5} m^2 and 2308 m, respectively. Figure 6b shows the histogram of the noise amplitudes. It is consistent with a Gaussian distribution, which validates the Gaussian probability density function of equation (6).

[20] Once the noise variance σ_d^2 and correlation distance a are estimated, the data covariance matrix C_d is determined from these values. The diagonal terms of the matrix correspond to σ_d^2 (single value for all the data points), and off-diagonal terms are calculated by considering the distance between points using equation (5) with the estimated values of σ_d^2 and a.

2.3. Model Appraisal

[21] The second stage of the neighborhood algorithm concerns the appraisal problem [*Sambridge*, 1999b], i.e., estimation of the model uncertainties. The method follows the framework of Bayesian inference (see *Tarantola* [1987] for a summary). It allows to calculate useful properties such as the mean model, posterior model covariance matrix, resolution matrix, or marginal posterior probability density functions.

[22] The Bayesian solution to an inverse problem is the posterior probability density function (PPD). When the Gaussian approximation is acceptable, the PPD can be written as

$$P(\mathbf{m}) = k \exp\left(-\frac{1}{2}\chi^2(\mathbf{m})\right), \tag{6}$$

where k is a normalizing constant and we assumed a uniform prior probability distribution. One of the key points of the method is that the PPD in a Voronoi cell around a point is represented by the PPD of that point. Namely, we accept a neighborhood approximation to the PPD as

$$P_{\mathrm{NA}}(\mathbf{m}) = P(\mathbf{p}_i), \tag{7}$$

where $\mathbf{p}_i$ is the closest point in those generated during the search stage to point $\mathbf{m}$ [*Sambridge*, 1999b]. Note that $P_{\mathrm{NA}}(\mathbf{m})$ is defined all over the model space. Bayesian integrals are then calculated from the approximated PPD by using a Monte Carlo integration technique. The technique used in the neighborhood algorithm numerically integrates functions by generating random points (Monte Carlo integration points) in the model space such that their distribution follows the approximated PPD [*Sambridge*, 1999b]. In our problem, 10,000 points are generated for Monte Carlo integrations with acceptable precision. At this stage, no further forward modeling is made.

[23] We calculate the mean model and marginal PPDs. The mean model of the ith parameter m_i is given by

$$\langle m_i \rangle = \int_{\mathcal{M}} m_i P_{\mathrm{NA}}(\mathbf{m}) d\mathbf{m}, \tag{8}$$

where the integral is taken in the model space $\mathcal{M}$. The marginal PPDs are, intuitively, projections of the posterior probability density to a model axis (one-dimensional) or to a model plane (two-dimensional). They are useful even when multiple maxima exist in the PPD. The one-dimensional marginal PPD of ith parameter is calculated by

$$M(m_i) = \int_{\mathcal{M}} P_{\mathrm{NA}}(\mathbf{m}) \prod_{\substack{k=1 \\ k \neq i}}^{d} dm_k, \tag{9}$$

and for the two-dimensional marginal PPD of ith and jth parameters,

$$M(m_i, m_j) = \int_{\mathcal{M}} P_{\mathrm{NA}}(\mathbf{m}) \prod_{\substack{k=1 \\ k \neq i,j}}^{d} dm_k. \tag{10}$$

The one-dimensional marginal PPDs provide the confidence intervals of the model parameters, while the two-dimensional counterparts provide additional information on trade-offs.

3. Synthetic Tests

[24] We perform some synthetic tests in order (1) to find a suitable value of the inversion parameter n and a suitable subsampling method and (2) to check the capabilities of the method. We test with four synthetic InSAR data sets that correspond to the two ascending and two descending data sets we have for the February 2000 eruption at Piton de la Fournaise. They are created by superposing exponential-type random noise to the line-of-sight displacements caused by a plausible model (which we call the "test model") for the eruption (Figure 7). Noise in each synthetic data is assumed to have the same variance and correlation length as those for the real data estimated in section 2.

3.1. Subsampling Method

[25] To make the misfit calculations manageable, we reduce the number of InSAR data points by subsampling. Here, we test how the subsampling method affects the inversion result. The first subsampling method interpolates the points on a regular 250 m side grid (Figure 8a). The second one distributes points circularly; points are concentrated in the vicinity of the eruptive fissures and become sparse in farther area (Figure 8b). The third one distributes points according to a quadtree algorithm [e.g., *Jónsson et al.*, 2002]; in our implementation, the points are created in such a way that the density roughly corresponds to the data amplitude (Figure 8c). The last one is such that the points correspond to the ground mesh nodes used to compute model displacements (Figure 8d). Except for the last one, model prediction is linearly interpolated to obtain the displacements on the subsampled points. For all the subsampled point sets, points on the recent lava flows are removed as we do not want to model them, making a total of 457, 369, 320, and 200 points for the regular, circular, quadtree and ground mesh node subsampling methods, respectively.

[26] The four synthetic InSAR data sets are subsampled and simultaneously inverted. It means that the length of the

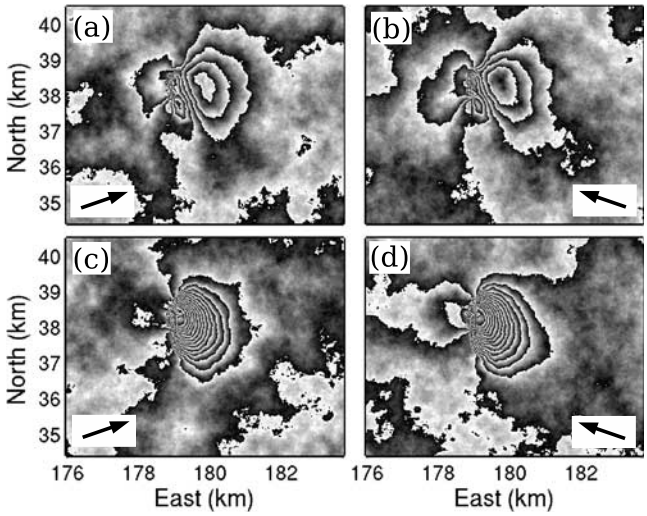

Figure 7. Synthetic data sets created by superposing exponential-type noise to modeled line-of-sight displacements caused by our test model. One shading cycle of black-gray-white corresponds to a displacement of 2.83 cm toward the satellite. Same line-of-sight directions as the actual InSAR data were assumed. Four data sets correspond to (a) F2N and (b) F4F (ascending) and (c) F3N and (d) F5F (descending) orbits. Arrows indicate the surface projection of the line-of-sight directions. See Table 3 for the line-of-sight vectors. See color version of this figure at back of this issue.

data and model vectors ($\mathbf{u}_o$ and $\mathbf{u}_m$ in equation (3)) is 4 times the number of subsampled data points. The inversion parameter n is set to 50; that is, 50 models are generated and evaluated in each iteration.

[27] Figure 9 shows the 95% confidence intervals determined from the one-dimensional marginal PPDs. The intervals estimated using the four subsampled data sets all include the test model as expected, indicating that all the subsampling methods are appropriate to our problem. We do not discuss here the differences in the length of the confidence intervals, because such small differences might come from the random nature of the Monte Carlo search method. However, for the overpressure (P_0), there is a systematic offset of the center of the confidence intervals from the test model; this is probably an effect of added noise. The maximum PPD (best fit) model is also plotted in Figure 9. It appears that the maximum PPD model does not necessarily coincide with the test model, mainly because of insufficient search within the maximum PPD region. This shows that determination of acceptable model ranges is more meaningful than obtaining a single optimum model.

3.2. Inversion Parameter

[28] As mentioned, the inversion parameter n controls the search behavior. We compare the results obtained using n = 10, 30, 50 and 70, in order to find a suitable value for our problem. The circular subsampled data set was used. Figure 9 shows that the test model is equally well retrieved by the maximum PPD model for the four cases. However, Figure 9 also shows that the confidence intervals of some parameters for n = 10 fail to include the test model. This is because the search was not extensive enough to find the global minimum. The results for n = 30, 50 and 70 do not show any significant difference.

[29] We decide to use n = 50 because (1) the risk of being caught in local minima is less than using smaller values, (2) large n leads to a better approximation of the PPD for the appraisal, and (3) the calculation time is manageable. Figure 10 shows how a search converges when n = 50 is taken. After about 20 iterations (1000 forward modelings), the search starts to focus toward the test model. The speed of convergence is different for each model parameter. The search characteristics for real applications are similar to this test result. One search run with n = 50 converges in about 20 hours on a Linux computer with a dual processor of 500 MHz. The appraisal normally takes several days on the same computer, but it can be shortened by running the program on several computers in parallel.

3.3. Marginal Probability Distributions

[30] In order to show the capability of the method, the marginal PPDs estimated using n = 50 and the circular data points are shown in Figure 11, together with the test, maximum PPD and mean models. The one-dimensional PPDs are quasi-symmetric and have a single peak. The similarity between the maximum PPD and mean models suggests symmetric and single-peaked distribution of the PPD also in the full seven-dimensional model space. The two-dimensional PPDs show insignificant trade-offs. The same type of confidence regions were obtained by *Cervelli et al.* [2002] using a bootstrap method for a dike intrusion problem at Kilauea volcano. Therefore quasi-symmetric and single-peaked characteristics of probability

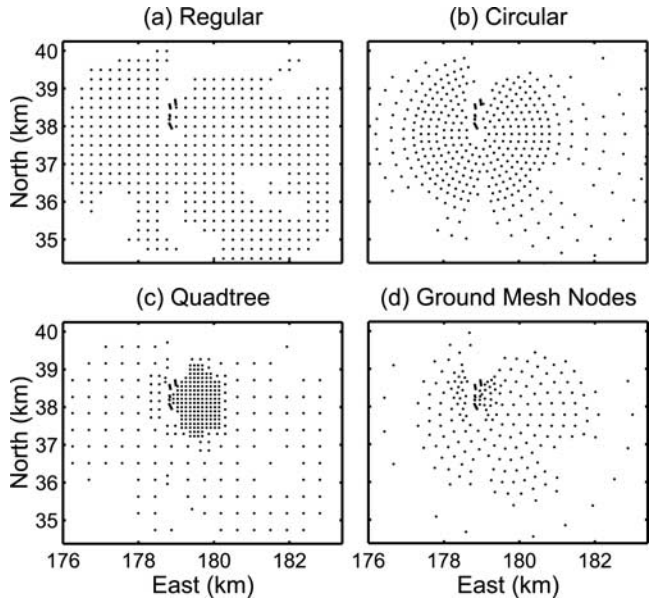

Figure 8. Points subsampled with different methods. (a) Regularly gridded points. (b) Circular points. (c) Points made with a quadtree algorithm. (d) Points coinciding with the ground mesh nodes (Figure 2). Locations of the eruptive fissures are indicated by solid lines. Areas without points correspond to recent lava flows where we do not have displacements associated with the dike intrusion.

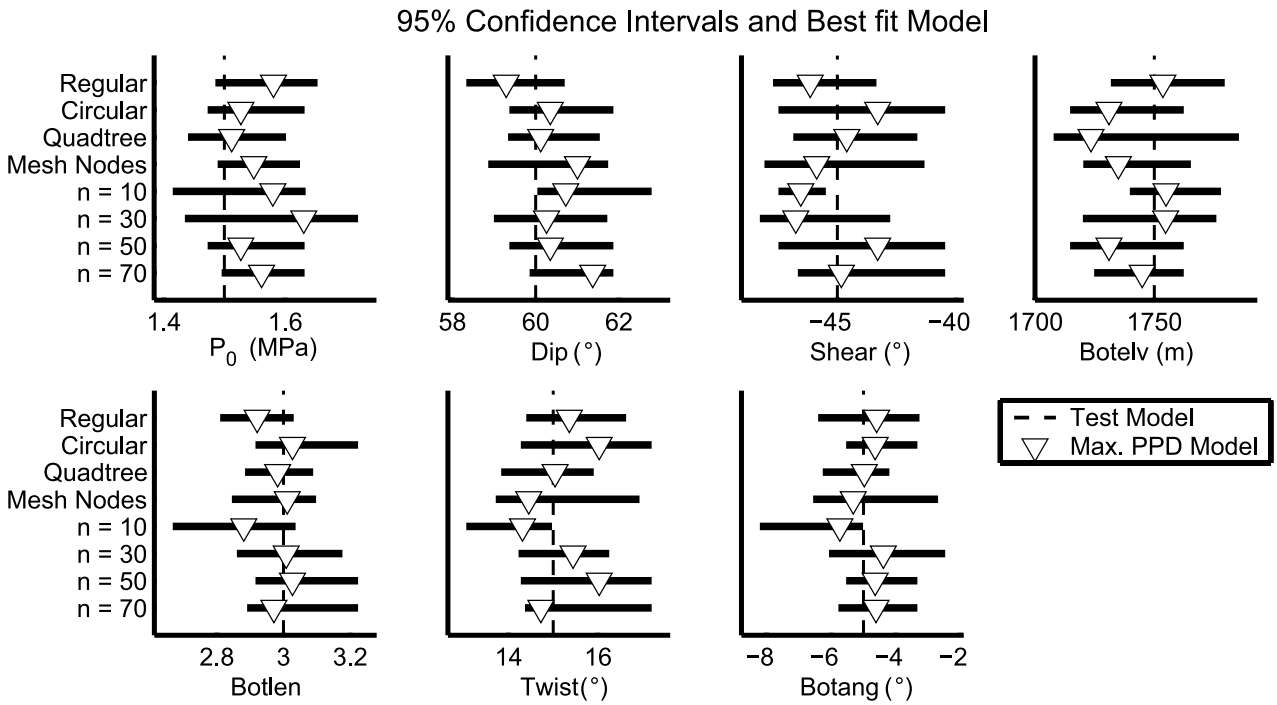

Figure 9. Maximum PPD (best fit) model and 95% confidence intervals (thick lines) determined from one-dimensional marginal PPDs, obtained using four subsampling methods (with $n = 50$) and different n values (with circular subsampling method). Dashed vertical lines indicate our test model. Estimation of confidence intervals is considered appropriate when the test model is within the confidence intervals.

distribution may be common characteristics in the inverse problems of ground deformation caused by dikes.

4. Application to the February 2000 Eruption at Piton de la Fournaise

4.1. Description of the Eruption

[31] Piton de la Fournaise is an active basaltic shield volcano of hot spot origin. It occupies the southeast of Réunion Island (France), situated 800 km east of Madagascar. The volcano has arcuated rift zones where eruptions and surface fractures are preferentially located (Figure 1). After 5 years of quiescence, the volcano entered a new cycle of activity in March 1998 with one of its largest eruptions of the last century. The February 2000 eruption was the fourth eruption in this cycle (Table 2). It occurred along the northern rift zone and caused a distinct seaward (eastward) displacements similar to that observed for the March 1998 eruption [*Sigmundsson et al.*, 1999]. At around 2315 LT on 13 February, changes in seismic activity and ground deformation were detected by the seismometer, tiltmeter and extensometer networks of the Observatoire Volcanologique

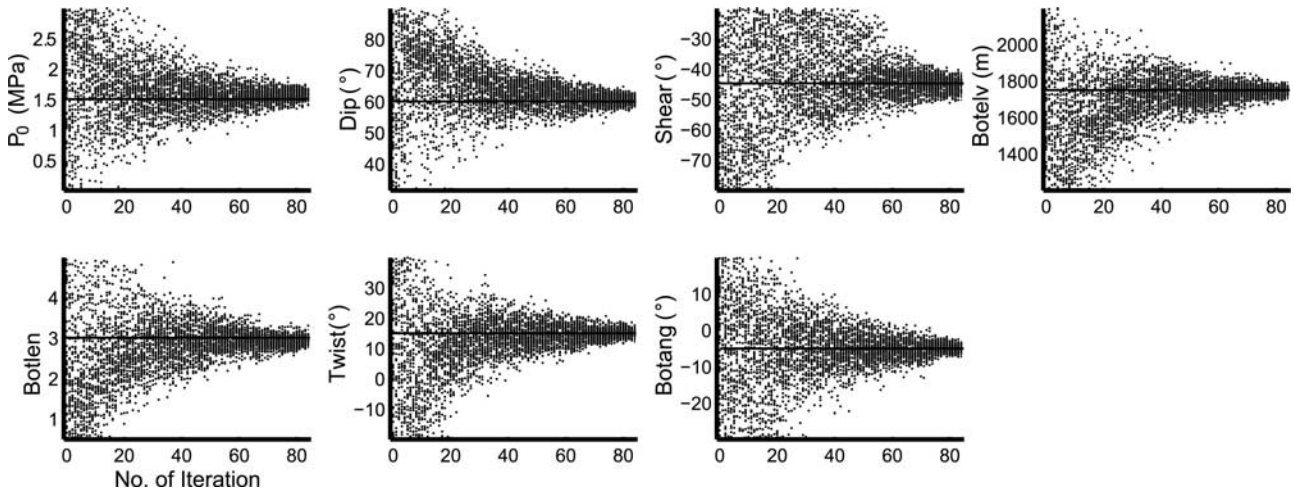

Figure 10. Parameter values plotted against number of iteration, in the case of a search with $n = 50$ using circularly subsampled synthetic data. Solid lines indicate the test model.

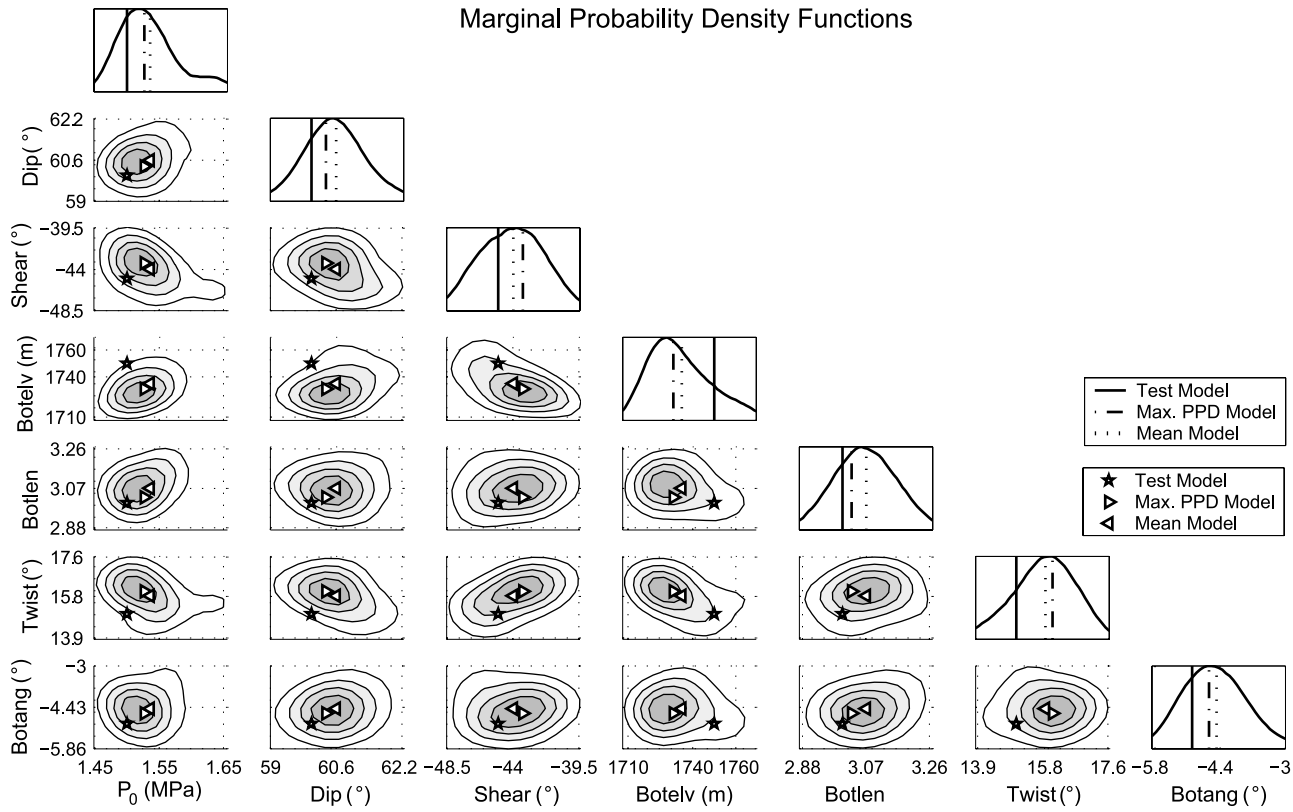

Figure 11. One-dimensional (diagonals) and two-dimensional (off-diagonals) marginal PPDs plotted with the test, maximum PPD and mean models, for the synthetic test with circular data points and $n = 50$. Contour interval is 0.2 times the maximum value.

du Piton de la Fournaise [*Staudacher et al.*, 2000]. The eruption started at 0018 LT on 14 February, about an hour after the detection of the precursors. The main eruptive activity quickly focused on the lowermost eruptive fissure and the eruption ceased at 1800 LT on 4 March.

4.2. Data

[32] RADARSAT-1 is a C-band satellite with 24 days of repeat time. Unlike the March 1998 eruption where a large number of images were available for one incidence angle before and after the eruption [*Sigmundsson et al.*, 1999], we only had a few images available because of the short interruption intervals before and after the eruption (Table 2). On the other hand, the archive offered different incidence angles both from ascending and descending orbits, which provides slightly different information on displacements. Four pairs of images with different incidence angles (Table 3) were found to be acceptable with respect to the time period and altitude of ambiguity [*Massonnet and Feigl*, 1998]. The interferograms were computed with DIAPASON software developed by French Centre National d'Etudes Spatiales. Topographic fringes were subtracted using a DEM provided by French Institut Géographique National. The altitudes of ambiguity indicate that the topographic effect on the interferograms is less than a tenth of a fringe. For one of the descending pairs (F3N), the azimuth spectrum was cut in Single Look Complex data to maximize the coherence and signal to noise ratio in the interferogram [*Durand et al.*, 2002].

[33] The four interferograms are shown in Figure 12a. The two ascending and two descending interferograms covering different time periods show similar displacements. Considering that the differences in the line-of-sight vectors are small, it suggests that there is negligible time-dependent deformation. The data clearly show asymmetric displacements: large displacements to the east and small displacements to the west of the eruptive fissures. The descending interferograms have about 14 fringes, indicating a maximum displacement toward the satellite of about 40 cm. The ascending data have 4 to 5 fringes, indicating

Table 2. Eruptions Since March 1998[a]

	Period	Eruptive Fissure Location	Lava Flow Volume, Mm^3
March 1998	9 March 1998 to 15 Sept. 1998	northern flank	40–50
July 1999	19 July 1999 to 31 July 1999	summit	1.8
Sept. 1999	28 Sept. 1999 to 23 Oct. 1999	summit/southern flank	1.5
Feb. 2000	14 Feb. 2000 to 4 March 2000	northern flank	6–8
June 2000	23 June 2000 to 30 July 2000	southeastern flank	10

[a] *Villeneuve* [2000].

Table 3. Interferograms Used in This Study

Orbit	Period	Line-of-Sight Vector [East, North, Up]	Incidence Angle, deg	h_a,[a] m
F2N (ascending)	7 Feb. 2000 to 13 May 2000	[−0.63, −0.17, 0.76]	40.7	−272.9
F4F (ascending)	14 Dec. 1999 to 19 March 2000	[−0.69, −0.19, 0.70]	45.7	−130.4
F3N (descending)	22 Oct. 1999 to 25 May 2000	[0.64, −0.17, 0.75]	41.8	−88.0
F5F (descending)	16 Dec. 1999 to 1 June 2000	[0.70, −0.19, 0.69]	46.8	494.1

[a]Altitude of Ambiguity.

a maximum displacement away from the satellite of about 14 cm. Subsidences associated with lava flow contractions are observed at the locations of the March 1998 and July and September 1999 lava flows.

[34] The interferograms were unwrapped with the SNAPHU unwrapping algorithm [*Chen and Zebker*, 2001]. The narrow fringes associated with a large displacement gradient in the descending interferograms did not allow a satisfactory unwrapping in a single calculation. Therefore the interferograms were unwrapped iteratively using the following algorithm: (1) unwrapping of the original interferogram, (2) low-pass filtering of the result with cutoff wavelength of about 500 m, (3) rewrapping of the filtered unwrapped data, (4) residual interferogram calculation by subtracting the phase of the rewrapped interferogram from that of the original interferogram, (5) unwrapping of the residual interferogram, (6) addition of the unwrapped data (product of (5)) to the product of (2), and (7) back to (2) or termination if the maximum amplitude is consistent with the number of fringes. Subsampled data sets were then created with the circular subsampling method after removing the speckles by low-pass filtering. Each of the four unwrapped data sets contains an unknown constant offset; this offset is adjusted automatically when evaluating the misfit so as to minimize the discrepancy between observed and modeled data.

4.3. Analysis

[35] We simultaneously invert the two ascending and two descending data sets, in order to search for the models that explain the four data sets equally well. This simultaneous inversion reduces the influence of atmospheric noise because each interferogram contains different noise. As decided from the synthetic tests, the number of models

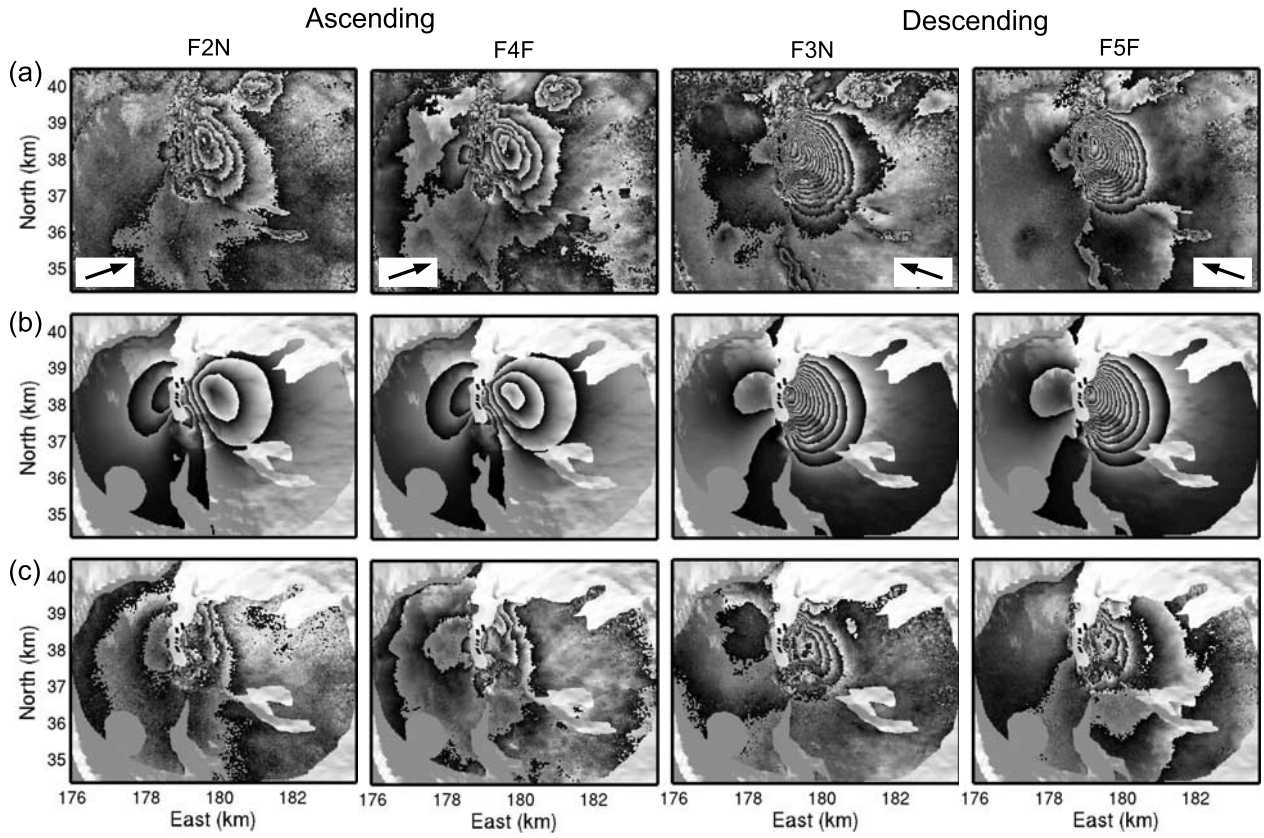

Figure 12. (a) Four interferograms indicating the ground displacements caused by the dike intrusion associated with the February 2000 eruption, superimposed on a DEM. Refer to the caption of Figure 7 for the meanings of gray scale shading and arrows and to Table 3 for data acquisition information. (b) Rewrapped modeled displacements for the four line-of-sight directions corresponding to the maximum PPD model. Recent lava flow areas not used in the misfit evaluation are masked out. (c) Residual displacements between observed and modeled data. See color version of this figure at back of this issue.

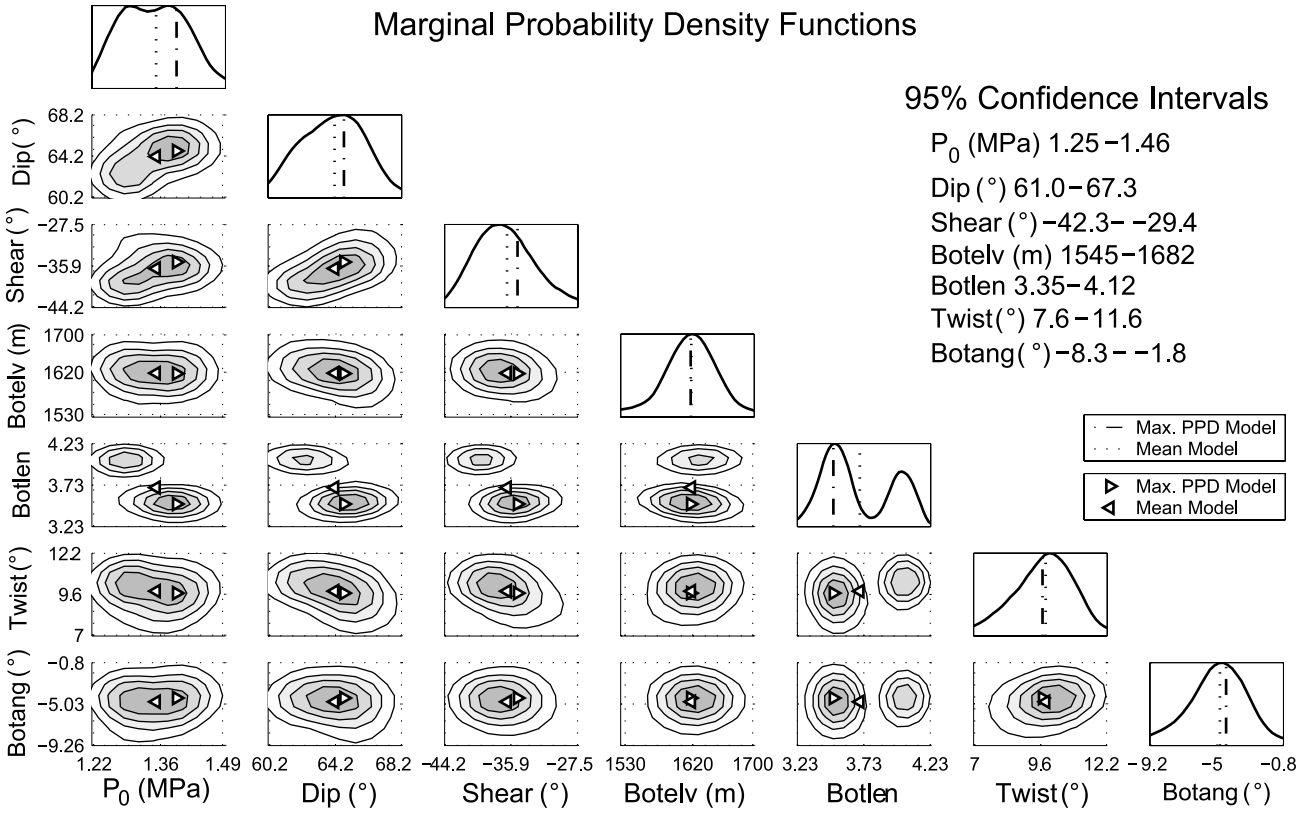

Figure 13. One- and two-dimensional marginal PPDs for the dike model. Contour interval is 0.2 times the maximum value. The 95% confidence intervals are also indicated. Parameters are well constrained with small uncertainties.

generated per iteration n is set to 50 in the search program.

4.3.1. Corrections to the Tested Models and the Misfit

[36] When a search finishes, we apply corrections to the overpressure and misfit values. As mentioned, overpressure correction is needed because a coarse dike mesh is used. The displacements for the maximum PPD model obtained with a coarse dike mesh are compared with those recalculated with a dense mesh to obtain the scaling factor. Then the overpressure of all the evaluated models is multiplied by the factor.

[37] A difference from the synthetic tests is that, in addition to the statistical uncertainties associated with data noise, we now have uncertainties which arise from the simplifications introduced by the model. These are taken into account by reestimating the data variance σ_d^2 used in the data covariance matrix. This correction is for the appraisal where the misfit is directly related to the probability density (equation (6)). In the search stage, the variance can be set to any value since the algorithm only uses the rank of the misfits. We first run a search with $\sigma_d^2 = 1$ and then rescale the resulting misfits by the variance calculated from the residual (observed minus best modeled) data. A typical reevaluated data variance is around 6×10^{-4} m^2, which is significantly larger than the variance of pure atmospheric noise (8.8×10^{-5} m^2).

4.3.2. Results

[38] Figures 12b and 12c show the modeled displacements for the maximum PPD model and residual displacements, respectively, corresponding to the four InSAR data sets. Comparisons are shown in the area where the circular subsampled points are placed. The model well explains the main characteristics of the observed data, such as limited displaced area east of the eruptive fissures (both ascending and descending data), a small lobe south of the fissures (ascending data), and little displacements west of the fissures (descending data). However, we observe some nonnegligible residuals. The model does not sufficiently explain the displacement asymmetry in the ascending directions. Also, three to four fringes of residuals are localized east of the eruptive fissures in the descending directions. Possible origins of the residuals are: atmospheric noise, oversimplification of the model, and other pressure sources such as a deflating deeper magma reservoir. Atmospheric noise can be ruled out as it is unlikely to have a strong atmospheric signal at the same place in the two independent interferograms of ascending or descending directions. The latter two possibilities are discussed later.

[39] The marginal PPDs (Figure 13) indicate that the model parameters are well constrained. For example, the 95% confidence intervals of the dip angle (Dip) and elevation of the middle point of the dike bottom side (Botelv) are as small as 6.3° and 137 m, respectively. We observe two peaks in the one- and two-dimensional marginal PPDs concerning Botlen, as well as minor trade-offs for some parameter pairs (e.g., Dip and P_0); however, these have little effect because of the small confidence intervals.

[40] The dike geometry of the maximum PPD model is shown in Figure 14. The geometries of all the acceptable models which have parameter values within the confidence

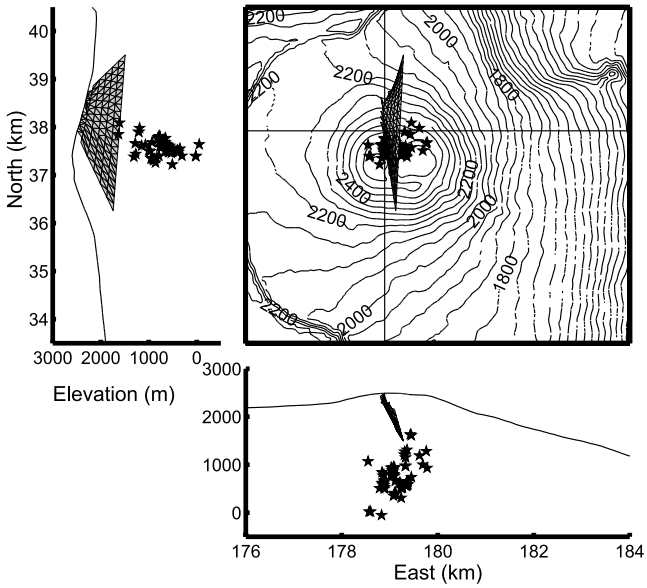

Figure 14. Map view and cross sections of the maximum PPD dike geometry, plotted with the hypocenters of the seismic swarm prior to the eruption [*Battaglia*, 2001]. The acceptable models have geometries similar to this because of the small model uncertainties.

intervals would be similar to Figure 14 because of the small model uncertainties. The acceptable models have common characteristics: a seaward dipping (61.0°–67.3°) trapezoid with its bottom passing 800–1000 m beneath the summit Dolomieu crater parallel to the rift zone. This result is in accordance with the seismicity and tilt data. Hypocenters of the seismic swarm showed an upward migration toward the summit (see Figure 14), while the tilt data indicated lateral propagation of magma from the summit area to the eruptive fissures [*Staudacher et al.*, 2000]. These data sets also suggest that magma reached the central to southern part of our estimated dike bottom and propagated laterally.

[41] Dikes open in response to the applied overpressure. The opening distribution for the maximum PPD model shows that the dike center opened by 59 cm (Figure 15). The average opening for the whole dike and that on the ground are 35 and 25 cm, respectively. The relatively small opening on the ground is attributed to the limited extent of the ground surface fissures. The average opening on the ground is consistent with the field observation of around 30 cm of openings (T. Staudacher, personal communication, 2003). Most of the old dike intrusions found at the bottom of deep eroded cliffs a few kilometers away from the summit have less than 1 m of thickness [*Grasso and Bachèlery*, 1995], which is consistent with our estimated value. The volume of the corresponding dike is estimated to be 6.5×10^5 m^3, which is about 6 times smaller than the estimated lava flow volume (4×10^6 m^3, *Staudacher et al.* [2000]).

5. Discussion

5.1. Influence of the Misfit Function Definition

[42] Our misfit function is controlled by the variance σ_d^2 and correlation length a of data noise. As estimation of these parameters inherently contains inaccuracy, it is important to know what we would obtain if different values were assumed.

[43] When a uniform variance and independency of data noise are assumed, the data covariance matrix becomes diagonal. In this case, the misfit function (equation (3)) becomes

$$\chi'^2(\mathbf{m}) = \frac{1}{\sigma_d^2} \sum^{N} (u_o - u_m)^2, \tag{11}$$

where N denotes the length of the data and model vectors. We tested the influence of this misfit definition and obtained a significantly different maximum PPD model (Dip = 54.0°, Botelv = 1790 m, Twist = 16.3°) from that obtained assuming correlated data noise. On the other hand, assuming a correlation length a = 1500 m (a plausible value for different atmospheric conditions) instead of 2308 m did not lead to significantly different maximum PPD model. From these tests, we conclude that considering data noise correlation has a significant effect, but the result is not very sensitive to the assumed correlation length. Note also that it is indispensable to take data noise correlation into account in the appraisal stage where the misfit values are meaningful.

[44] The data variance σ_d^2 also affects the appraisal; the larger the value, the broader the confidence intervals. We investigated its influence by assuming half the data variance used in the analysis. We obtained confidence intervals that are only 71% shorter on average for the seven parameters, indicating that the data variance has a limited impact on the confidence intervals.

5.2. Comparisons With Simpler Models

[45] Many dike modeling studies using ground deformation data assume a rectangular dislocation in elastic half-space [*Okada*, 1985]. In order to compare this model with the three-dimensional mixed BEM, an inversion is performed using Okada's equations. Model parameters are the opening (uniform), location (three parameters), length, width, dip angle and strike angle. We use the same inversion method and same data set as before.

[46] Table 4 compares the maximum PPD Okada model with that obtained by our method. The length and strike of the Okada model are close to those at the top of the mixed

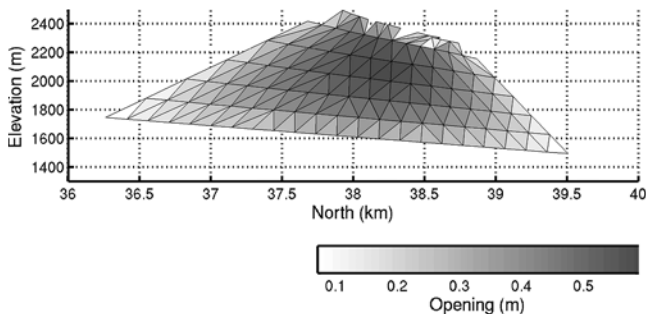

Figure 15. Opening of the dike in response to the constant overpressure for the maximum PPD model. The maximum opening is 59 cm, the average on the whole area and that on the ground surface are 35 and 25 cm, respectively.

Table 4. Maximum PPD Mixed BEM and Okada Models

	Opening, cm	Dip, deg	Length, m	Bottom Depth, m	Strike, °N	Area, Mm^2	Volume, Mm^3
Mixed BEM	35	64.7	930–3257	745	12.5–2.8	1.8	0.65
Okada	63	67.0	1182	1029	12.2	1.3	0.79

For the mixed BEM model, opening and bottom depth are given in average, length and strike are given in dike top, bottom values. Top of the Okada model is estimated at 51 m below the ground.

BEM model, suggesting that Okada-type models tend to predict the geometry close to the ground and poorly predict the geometry at depth. Indeed, the dike bottom depth is 38% greater than the average depth of the mixed BEM model. Moreover, it gives an opening 80% larger than the averaged opening of the BEM model. This is partly because Okada's model predicts the dike area where opening is large. If we calculate the average opening of the mixed BEM model on an area similar to the Okada model, we get 48 cm, in which case the discrepancy reduces to 30%. The resulting displacements (Figure 16a) are significantly different from the observed data (Figure 12a). There are too many fringes west of the eruptive fissures, and the displacement patterns are too elongated to east-west direction.

[47] Some more detailed studies assume a realistic opening distribution rather than a uniform opening by considering a number of Okada-type rectangular segments [*Aoki et al.*, 1999; *Amelung et al.*, 2000]. These studies do not generally estimate the dike geometry and opening distribution simultaneously, but if they did, they would obtain a similar model to that obtained by the mixed BEM with a flat ground surface assumption. An inversion is performed for a flat ground surface at the elevation of 2300 m. The maximum PPD model has significantly different values of P_0, Botelv, Botlen and Botang than the model with realistic topography (Table 5). The overpressure P_0 is overestimated by 24%. The last three parameters are related to the dike bottom; in this particular case, the bottom deepens toward south instead of north and reaches 934 m above sea level at its southern edge (compare with Figure 14). The difference in Botelv (the elevation of the middle point of the bottom line) is about 300 m, which corresponds to about 30% of difference in the dike height. The similar degree of discrepancies to those for the Okada model suggests that part of the differences found with the Okada model originate from neglecting the topography. The modeled displacements (Figure 16b) are still too elongated in the east-west direction.

5.3. Model Assumptions

[48] We assumed that the edifice is homogeneous, isotropic and linearly elastic. Since relaxing these assumptions lead to different prediction of ground displacements, such assumptions might bias the dike model estimation.

[49] A tomographic study [*Nercessian et al.*, 1996] indicates a high velocity plug of 1.5 km in diameter below the summit crater, surrounded by a lower-velocity ring. This is the most distinct heterogeneity that we expect around the depth we are concerned with. The InSAR fringes are uncorrelated to this potential plug and ring structure, suggesting that the homogeneity assumption is valid. The effects of local heterogeneities due to individual dike intrusions etc. are averaged out by considering effective elastic moduli.

[50] Anisotropy can be caused by stratified lava flows. *Ryan et al.* [1983] estimated a 1.4 times greater Young's modulus in the horizontal direction than in the vertical direction at Kilauea volcano. Such anisotropy could be responsible for the observed asymmetric displacements between the eastern and western sides of the eruptive fissures. However, our studied area has many intruded dikes that locally cause anisotropy in different directions. Thus it is not clear what kind of anisotropy model is appropriate to our problem.

[51] Inelastic deformation generally occurs close to the eruptive fissures. We do not observe any systematic residual displacements correlated to the fissure locations, probably because we masked the area close to the fissures. Thus inelastic effects do not affect our result.

[52] Volcanic edifices are expected to have complex stress fields due to surface topography, material heterogeneities associated with previous dike intrusions, etc. Therefore the constant dike overpressure assumed in this study is probably an oversimplification. A vertical overpressure gradient would give a better approximation; however, a preliminary study showed that this overpressure gradient cannot be constrained by the inversion, suggesting that such a model does not describe the reality any better than the constant overpressure model. We probably need to consider a

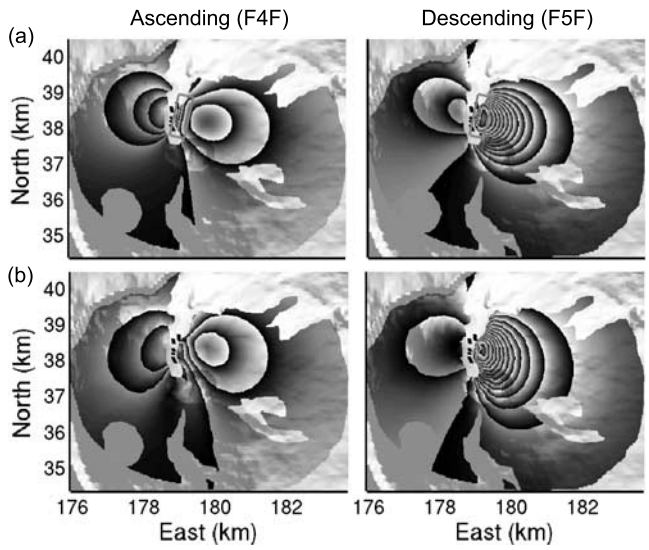

Figure 16. Rewrapped maximum PPD displacements modeled using (a) Okada's equations and (b) the mixed BEM with a flat ground surface, in an ascending (F4F) and a descending (F5F) directions. Gray rectangle line in Figure 16a indicates the projected model geometry. A set of small Okada-type segments with different opening values would create similar displacements as those shown in Figure 16b. See color version of this figure at back of this issue.

Table 5. Maximum PPD Mixed BEM Models With Realistic and Flat Topographies

	P_0, MPa	Dip, deg	Shear, deg	Botelv, m	Botlen	Twist, deg	Botang, deg	Area, Mm^2	Volume, Mm^3
Realistic	1.3	64.7	−35.1	1617	3.50	9.7	−4.4	1.8	0.65
Flat	1.7	68.4	−35.7	1333	3.97	10.5	13.2	2.1	0.81

more complex overpressure distribution as well as a shear stress distribution, for instance by taking into account the stress associated with topography [*Pinel and Jaupart*, 2004].

[53] The top of the dike was fixed at the locations of the eruptive fissures in our modeling, while the ascending data (Figure 12a) seem to indicate that the superficial fissures extend further to the north. However, simple extension of the dike top by 500 m did not lead to a better fit. Extension of the dike to the south was also tested by adding a vertex between the southern top and bottom vertexes of the quadrangle, which makes the dike model to be pentagonal (nine dike geometry parameters), but the optimum model was similar to that obtained by the quadrangle model. These tests suggest that the data residuals are not caused by an error in the location of the dike top.

5.4. Effect of a Basal Plane

[54] The horseshoe-shaped depression of Enclos-Fouqué caldera has been interpreted by several authors as the head wall of an eastward moving landslide [e.g., *Lénat et al.*, 2001]. This idea is supported by the age and volume of landslide materials found on the submarine eastern flank of the volcano [*Labazuy*, 1996], though the landslides may have been restricted to the area close to the ocean [e.g., *Merle and Lénat*, 2003].

[55] In order to test the hypothesis that reactivation of the basal plane of the caldera caused the observed asymmetric displacement pattern, such a plane is modeled with the mixed BEM (Figure 17a). We assume that the eastern part is freely slipping in response to the dike inflation so that it has a null stress boundary condition. The western part is assumed to be locked so that it is not modeled. The dike is assumed to be vertical only to see the effect of the plane. The basal plane is connected to the ground at sea level on the east end, and to the dike at 700 m above sea level so that the westward extension of the plane reaches the caldera wall.

[56] Modeled displacements with the basal plane (Figure 17c) have a larger wavelength pattern than those without it (Figure 17b). This is inconsistent with the InSAR data. In addition, preliminary inversions with a rectangular slip plane (seaward dip and elevation of the plane are additional model parameters) beneath the dike did not indicate any better fit to the data. We therefore conclude that the observed asymmetric displacement patterns were not caused by a basal plane slip but, as we found, by the dip of the dike.

5.5. Magma Transfer System

[57] We showed with a high confidence that the dike bottom side lies 800 to 1000 m below the ground. The preeruption seismic swarm (Figure 14) indicates that the dike intrusion started around sea level (2600 m below the summit), and that magma came from a greater depth. This leads to two questions: (1) Where was the source of magma that fed the eruption located? and (2) Why is the estimated dike model significantly shallower than what is expected from the seismic swarm?

[58] An answer to the first question can be deduced from the fact that the InSAR data do not indicate any deflation source that accounts for the lava flow and dike volumes. Geodetic measurements rarely find a deflation source that accounts for the erupted and intruded magma volume [*Owen et al.*, 2000; *Amelung and Day*, 2002], but this may be due to limited detectability of signals.

[59] In order to determine the minimum depth for the source of magma to cause undetectable surface displacements, we assume that the volume leaving the magma reservoir (Vr) and the erupted/intruded volume (Ve) balance. The major factors that affect the magma balance are: (1) magma degassing during ascent, (2) lava contraction associated with cooling, and (3) vesicles and cavities in the lava flow. The first factor leads to Vr > Ve by a few percent [*Tait et al.*, 1989], the second one to Vr > Ve by 10–15% [*Yoder*, 1976], and the last one to Vr < Ve by roughly 20–50% [*Cas and Wright*, 1987]; in all, the magma balance assumption is roughly valid.

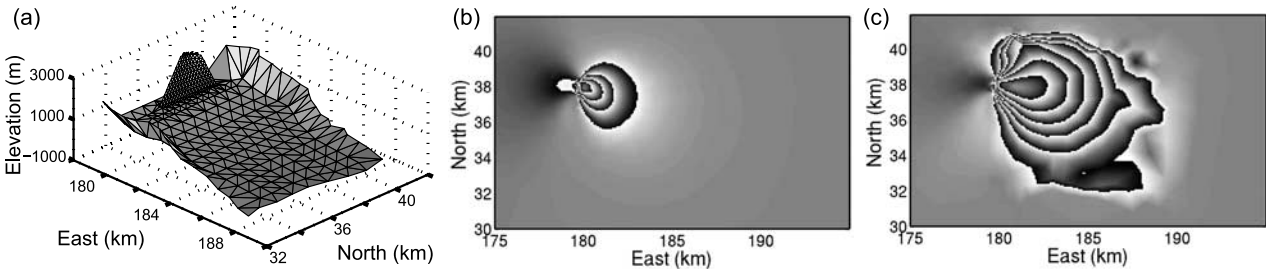

Figure 17. (a) Dike and basal plane meshes used to evaluate the effect of a basal plane. See text for explanations. (b) Line-of-sight displacements in a descending direction (F5F) modeled without the basal plane. A small overpressure 0.13 MPa was assumed for a better display of the results. (c) Displacements modeled with the basal plane. The same line-of-sight direction and overpressure as Figure 17b were assumed. Note that the basal plane creates a seaward slip of a larger wavelength.

[60] We modeled a spherical deflation source using the mixed BEM, with a diameter of 1000 m and a volume loss equal to the sum of the lava flow and dike volumes (4.7×10^6 m^3). It should be noted that the modeled displacements are mainly sensitive to the magma reservoir volume change, and insensitive to the reservoir dimension at the considered depth. We found that if the center of the source was located deeper than 3000 m below sea level, it would create less than one fringe along the line-of-sight directions. Such a small fringe could be hidden by those created by the dike intrusion and atmospheric noise. Consequently, the source of magma should be located deeper than 3000 m below sea level (5600 m beneath the summit).

[61] To answer the second question; that is, to explain the depth difference between the preeruption seismic swarm and the dike model, two scenarios are possible. The first one is that magma intruded through a path too narrow to cause detectable displacements on InSAR data. Such a narrow path is suggested by *Amelung and Day* [2002] on Fogo volcano, Cape Verde, where InSAR data for the 1995 eruption did not show any evidence of a shallow magma reservoir as in our case. The second one is that the deeper magma path closed once the eruption ceased. This scenario is possible if magma withdrew from the path back into the magma reservoir or if magma ascended by buoyancy after the overpressure in the magma reservoir was relaxed [*Dahm*, 2000].

[62] *Lénat and Bachèlery* [1990] proposed a shallow storage system that consists of discrete magma pockets on the basis of the diversity of preeruptive seismicity and tilt changes. Petrological characteristics of lavas emitted in recent 25 years are in accordance with their model [*Boivin and Bachèlery*, 2003]. Taking into account our consideration, such a system may exist provided that magma in shallow pockets is pushed toward the ground by the arrival of magma from depth. If the densities of the two magmas are the same, such a mechanism would create no deformation.

[63] To further investigate the magma transfer system, a comprehensive study of seismicity and continuous geodetic data is needed. An interesting feature worth noting in addition is that the upper limit of the hydrothermal system has been identified by a geoelectrical study at a few hundred meters beneath the summit area of the volcano [*Lénat et al.*, 2000], which is consistent with the depth of our model. It suggests that the hydrothermal system might play a role in the magma propagation behavior.

5.6. What Controls the dip of the Dike?

[64] The inversion results and the discussion on the basal plane strongly suggests a $61.0°-67.3°$ seaward dipping dike. Interferograms for other dike intrusions along the northern rift zone of Piton de la Fournaise show similar asymmetric pattern [*Sigmundsson et al.*, 1999; *Froger et al.*, 2004], suggesting similar dip angles. This indicates that the minimum principal stress along the rift zone on the northern flank of the volcano is in east-west direction and inclined about 25° vertically (the normal direction of the dike surface). Such a stress condition may be associated with a weakness area created by gravitational instability, though further studies are needed to unravel the mechanism. This is fundamental to the formation of the rift zones of Piton de la Fournaise and hence is a key point to predict the future development of the volcano.

6. Conclusions

[65] We showed that a combination of InSAR data, a three-dimensional mixed boundary element method and a neighborhood algorithm inversion gives detailed and reliable information on a dike intrusion. Inversions with synthetic data showed that a test model can be well retrieved by the inversion method within predicted uncertainties, and that all the tested subsampling methods are acceptable for our dike intrusion problem. For the InSAR data, the marginal probability density functions of model parameters indicate small uncertainties and trade-offs. Incorporating data noise correlation is found to be important; a misfit function that takes this into account leads to a significantly different maximum PPD (best fit) model.

[66] The acceptable models of the dike intrusion at Piton de la Fournaise well explain the main characteristics of the InSAR data. The maximum PPD dike model predicts an average ground opening of 25 cm, consistent with field observation. Acceptable models share common characteristics: a seaward dipping ($61.0°-67.3°$) trapezoid with its bottom passing 800–1000 m beneath the summit Dolomieu crater parallel to the rift zone.

[67] Models that neglect the topography, including a single rectangular dislocation model, poorly estimate overpressure (or opening) and geometry at depth. Overestimations in overpressure (or opening) and dike height amount to about 30%, and in volume to about 20%. This indicates the importance of taking realistic topography into account. A model with a basal slip plane, which may exist under Enclos-Fouqué caldera, shows that the dike inflation did not reactivate the plane, and that the observed asymmetric displacements are solely attributed to the dipping dike. The magma which supplied the eruption should be sourced deeper than 3000 m below sea level (5600 m beneath the summit), considering the fact that the observed data do not indicate any deflation source. Taking into account the lack of inflation related to a magma path from the source and the estimated dike, we propose one of the following feeding systems: (1) a narrow path or (2) a path that closes once an eruption ceases.

[68] This detailed and careful analysis gives constraints on the mechanisms of the magma transfer system and formation of the rift zones. Further analyses of InSAR data for other eruptions and incorporation of other kinds of data could provide a better understanding on the eruption behavior and structure of the volcano.

[69] **Acknowledgments.** We are grateful to the Canadian Space Agency for the RADARSAT-1 data provided through ADRO2 253 and to D. Massonnet for launching the project. We thank M. Sambridge for his NA inversion codes, J.-L. Froger for suggestions in interferogram unwrapping and the ground meshing program, T. Souriot for his help on unwrapping, P. Boivin for discussions on the volcano magma system, and J. Battaglia for the seismicity data. We also thank F. Cornet, J.-F. Lénat, and A. Provost for reviewing the manuscript before submission and B. van Wyk de Vries for reviewing and English improvement before and after submission. Long and thoughtful comments of the three reviewers (two anonymous and Sigurjón Jónsson) and the Associate Editor L. Mastin contributed to improve the quality of the paper.

References

Amelung, F., and S. Day (2002), InSAR observations of the 1995 Fogo, Cape Verde, eruption: Implications for the effects of collapse events upon island volcanoes, *Geophys. Res. Lett.*, *29*(12), 1606, doi:10.1029/2001GL013760.

Amelung, F., S. Jónsson, H. Zebker, and P. Segall (2000), Widespread uplift and 'trapdoor' faulting on Galàpagos volcanoes observed with radar interferometry, *Nature*, *407*, 993–996.

Aoki, Y., P. Segall, T. Kato, P. Cervelli, and S. Shimada (1999), Imaging magma transport during the 1997 seismic swarm off the Izu Peninsula, Japan, *Science*, *286*, 927–930.

Battaglia, J. (2001), Quantification sismique des phénomènes magmatiques sur le Piton de la Fournaise entre 1991 et 2000, thèse de doctrat, Univ. Paris 7 Denis Diderot, Paris, France.

Beauducel, F., and F. H. Cornet (1999), Collection and three-dimensional modeling of GPS and tilt data at Merapi volcano, Java, *J. Geophys. Res.*, *104*, 725–736.

Boivin, P., and P. Bachèlery (2003), The behaviour of the shallow plumbing system at La Fournaise volcano (Réunion Island). A petrological approach, paper presented at EGS-AGU-EUG Joint Assembly, Nice, France.

Cas, R. A. F., and J. V. Wright (1987), *Volcanic Successions*, CRC Press, Boca Raton, Fla.

Cayol, V., and F. H. Cornet (1997), 3D mixed boundary elements for elastostatic deformation fields analysis, *Int. J. Rock Mech. Min. Sci. Geomech. Abstr.*, *34*, 275–287.

Cayol, V., and F. H. Cornet (1998), Three-dimensional modeling of the 1983–1984 eruption at Piton de la Fournaise Volcano, Reunion Island, *J. Geophys. Res.*, *103*, 18,025–18,037.

Cayol, V., J. H. Dieterich, A. Okamura, and A. Miklius (2000), High magma storage rates before the 1983 eruption of Kilauea, Hawaii, *Science*, *288*, 2343–2346.

Chen, C. W., and H. A. Zebker (2001), Two-dimensional phase unwrapping with use of statistical models for cost functions in nonlinear optimization, *J. Opt. Soc. Am.*, *18*, 338–351.

Cervelli, P., M. H. Murray, P. Segall, Y. Aoki, and T. Kato (2001), Estimating source parameters from deformation data, with an application to the March 1997 earthquake swarm off the Izu Peninsula, Japan, *J. Geophys. Res.*, *106*, 11,217–11,237.

Cervelli, P., P. Segall, F. Amelung, H. Garbeil, C. Meertens, S. Owen, A. Miklius, and M. Lisowski (2002), The 12 September 1999 Upper East Rift Zone dike intrusion at Kilauea Volcano, Hawaii, *J. Geophys. Res.*, *107*(B7), 2150, doi:10.1029/2001JB000602.

Crouch, S. L., and A. M. Starfield (1983), *Boundary Element Methods in Solid Mechanics*, Allen and Unwin, London.

Dahm, T. (2000), On the shape and velocity of fluid-filled fractures in the Earth, *Geophys. J. Int.*, *142*, 181–192.

Dieterich, J., V. Cayol, and P. Okubo (2000), The use of earthquake rate changes as a stress meter at Kilauea volcano, *Nature*, *408*, 457–460.

Durand, P., M. van der Kooij, and F. Adragna (2002), An update in the evolution of Radarsat1 Azimuth Doppler for differential interferometry purposes, paper presented at Colloques International Geoscience and Remote Sensing Symposium, Geosci. and Remote Sens. Soc., Toronto, Canada.

Froger, J. L., Y. Fukushima, P. Briole, T. Staudacher, T. Souriot, and N. Villeneuve (2004), The deformation field of the August 2003 eruption at Piton de la Fournaise, Reunion Island, mapped by ASAR interferometry, *Geophys. Res. Lett.*, *31*, L14601, doi:10.1029/2004GL020479.

Fukushima, Y., O. Nishizawa, H. Sato, and M. Ohtake (2003), Laboratory study on scattering characteristics in rock samples, *Bull. Seismol. Soc. Am.*, *93*, 253–263.

Grasso, J. R., and P. Bachèlery (1995), Hierarchical organization as a diagnostic approach to volcano mechanics: Validation on Piton de la Fournaise, *Geophys. Res. Lett.*, *22*, 2897–2900.

Jónsson, S., H. Zebker, P. Segall, and F. Amelung (2002), Fault slip distribution of the 1999 M_w 7.1 Hector Mine, California, earthquake, estimated from satellite radar and GPS measurements, *Bull. Seismol. Soc. Am.*, *92*, 1377–1389.

Labazuy, P. (1996), Recurrent landslides events on the submarine flank of Piton de la Fournaise volcano (Reunion Island), in *Volcano Instability on the Earth and Other Planets*, edited by W. J. McGuire, A. P. Jones, and J. Neuberg, *Geol. Soc. Spec. Publ.*, *110*, 295–306.

Lénat, J.-F., and P. Bachèlery (1990), Structure et fonctionnement de la zone centrale du Piton de la Fournaise, in *Le voicanisme de la Réunion*, edited by J.-F. Lénat, pp. 257–296, Cent. de Rech. Volcanol., Clermont-Ferrand, France.

Lénat, J.-F., D. Fitterman, and D. B. Jackson (2000), Geoelectrical structure of the central zone of Piton de la Fournaise volcano (Réunion), *Bull. Volcanol.*, *62*, 75–89.

Lénat, J.-F., B. Gilbert-Malengreau, and A. Galdéano (2001), A new model for the evolution of the volcanic island of Réunion (Indian Ocean), *J. Geophys. Res.*, *106*, 8645–8663.

Lohman, R. B., M. Simons, and B. Savage (2002), Location and mechanism of the Little Skull Mountain earthquake as constrained by satellite radar interferometry and seismic waveform modeling, *J. Geophys. Res.*, *107*(B6), 2118, doi:10.1029/2001JB000627.

Massonnet, D., and K. L. Feigl (1998), Radar interferometry and its application to changes in the Earth's surface, *Rev. Geophys.*, *36*, 441–500.

Masterlark, T. (2003), Finite element model predictions of static deformation from dislocation sources in a subduction zone: Sensitivities to homogeneous, isotropic, Poisson-solid, and half-space assumptions, *J. Geophys. Res.*, *108*(B11), 2540, doi:10.1029/2002JB002296.

Merle, O., and J.-F. Lénat (2003), Hybrid collapse mechanism at Piton de la Fournaise volcano, Reunion Island, Indian Ocean, *J. Geophys. Res.*, *108*(B3), 2166, doi:10.1029/2002JB002014.

Mogi, K. (1958), Relations between the eruptions of various volcanoes and the deformation of the ground surfaces around them, *Bull. Earthquake Res. Inst. Univ. Tokyo*, *36*, 99–134.

Nercessian, A., A. Hirn, J.-C. Lepine, and M. Sapin (1996), Internal structure of Piton de la Fournaise volcano from seismic wave propagation and earthquake distribution, *J. Volcanol. Geotherm. Res.*, *70*, 123–143.

Okada, Y. (1985), Surface deformation due to shear and tensile faults in a half-space, *Bull. Seismol. Soc. Am.*, *75*, 1135–1154.

Owen, S., P. Segall, M. Lisowski, A. Miklius, M. Murray, M. Bevis, and J. Foster (2000), January 30, 1997 eruptive event on Kilauea Volcano, Hawaii, as monitored by continuous GPS, *Geophys. Res. Lett.*, *27*, 2757–2760.

Pinel, V., and C. Jaupart (2004), Magma storage and horizontal dyke injection beneath a volcanic edifice, *Earth Planet. Sci. Lett.*, *221*, 245–262.

Pritchard, M. E., and M. Simons (2002), A satellite geodetic survey of large-scale deformation of volcanic centres in the central Andes, *Nature*, *418*, 167–171.

Rançon, J.-P., P. Lerebour, and T. Auge (1989), The Grand-Brulé exploration drilling: New data on the deep framework of the Piton de la Fournaise volcano. Part 1: Lithostratigraphic units and volcanostructural implications, *J. Volcanol. Geotherm. Res.*, *36*, 113–127.

Ryan, M. P., J. Y. K. Blevins, A. T. Okamura, and R. Y. Koyanagi (1983), Magma reservoir subsidence mechanics: Theoretical summary and application to Kilauea Volcano, Hawaii, *J. Geophys. Res.*, *88*, 4147–4181.

Sambridge, M. (1999a), Geophysical inversion with a neighbourhood algorithm: I. Searching a parameter space, *Geophys. J. Int.*, *138*, 479–494.

Sambridge, M. (1999b), Geophysical inversion with a neighbourhood algorithm: II. Appraising the ensemble, *Geophys. J. Int.*, *138*, 727–746.

Sigmundsson, F., P. Durand, and D. Massonnet (1999), Opening of an eruptive fissure and seaward displacement at Piton de la Fournaise Volcano measured by RADARSAT satellite radar interferometry, *Geophys. Res. Lett.*, *26*, 533–536.

Staudacher, T., N. Villeneuve, J.-L. Cheminée, K. Aki, J. Battaglia, P. Catherine, V. Ferrazzini, and P. Kowalski (2000), Piton de la Fournaise, *Bull. Global Volcanism Network*, *25*, 14–16.

Tait, S., C. Jaupart, and S. Vergniolle (1989), Pressure, gas content and eruption periodicity of a shallow crystallising magma chamber, *Earth Planet. Sci. Lett.*, *92*, 107–123.

Tarantola, A. (1987), *Inverse Problem Theory*, Elsevier, New York.

Villeneuve, N. (2000), Apports multi-sources à une meilleure compréhension de la mise en place des coulées de lave et des risques associés au Piton de la Fournaise, thèse de doctorat, Inst. de Phys. du Globe de Paris, Paris, France.

Wright, T. J., Z. Lu, and C. Wicks (2003), Source model for the M_w 6.7, 23 October 2002, Nenana Mountain Earthquake (Alaska) from InSAR, *Geophys. Res. Lett.*, *30*(18), 1974, doi:10.1029/2003GL018014.

Yoder, H. S. (1976), *Generation of Basaltic Magma*, Natl. Acad. Sci., Washington, D. C.

V. Cayol and Y. Fukushima, Laboratoire Magmas et Volcans, Université Blaise Pascal, CNRS UMR 6524, 5 rue Kessler, F-63038 Clermont-Ferrand, France. (valerie.cayol@opgc.univ-bpclermont.fr; yofukushima@opgc.univ-bpclermont.fr)

P. Durand, Centre National d'Etudes Spatiales, 18 Avenue E. Belin, F-31055 Toulouse, France. (philippe.durand@cnes.fr)

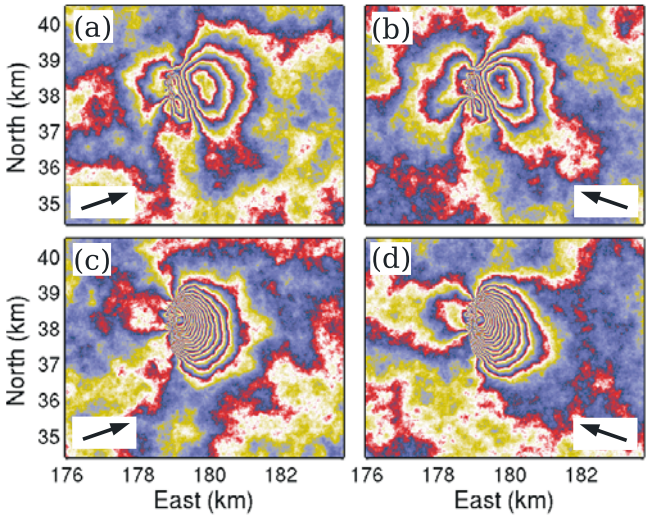

Figure 7. Synthetic data sets created by superposing exponential-type noise to modeled line-of-sight displacements caused by our test model. One shading cycle of black-gray-white corresponds to a displacement of 2.83 cm toward the satellite. Same line-of-sight directions as the actual InSAR data were assumed. Four data sets correspond to (a) F2N and (b) F4F (ascending) and (c) F3N and (d) F5F (descending) orbits. Arrows indicate the surface projection of the line-of-sight directions. See Table 3 for the line-of-sight vectors.

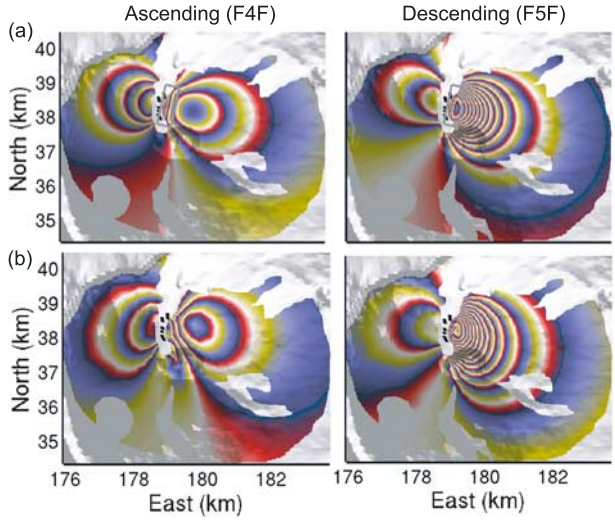

Figure 16. Rewrapped maximum PPD displacements modeled using (a) Okada's equations and (b) the mixed BEM with a flat ground surface, in an ascending (F4F) and a descending (F5F) directions. Gray rectangle line in Figure 16a indicates the projected model geometry. A set of small Okada-type segments with different opening values would create similar displacements as those shown in Figure 16b.

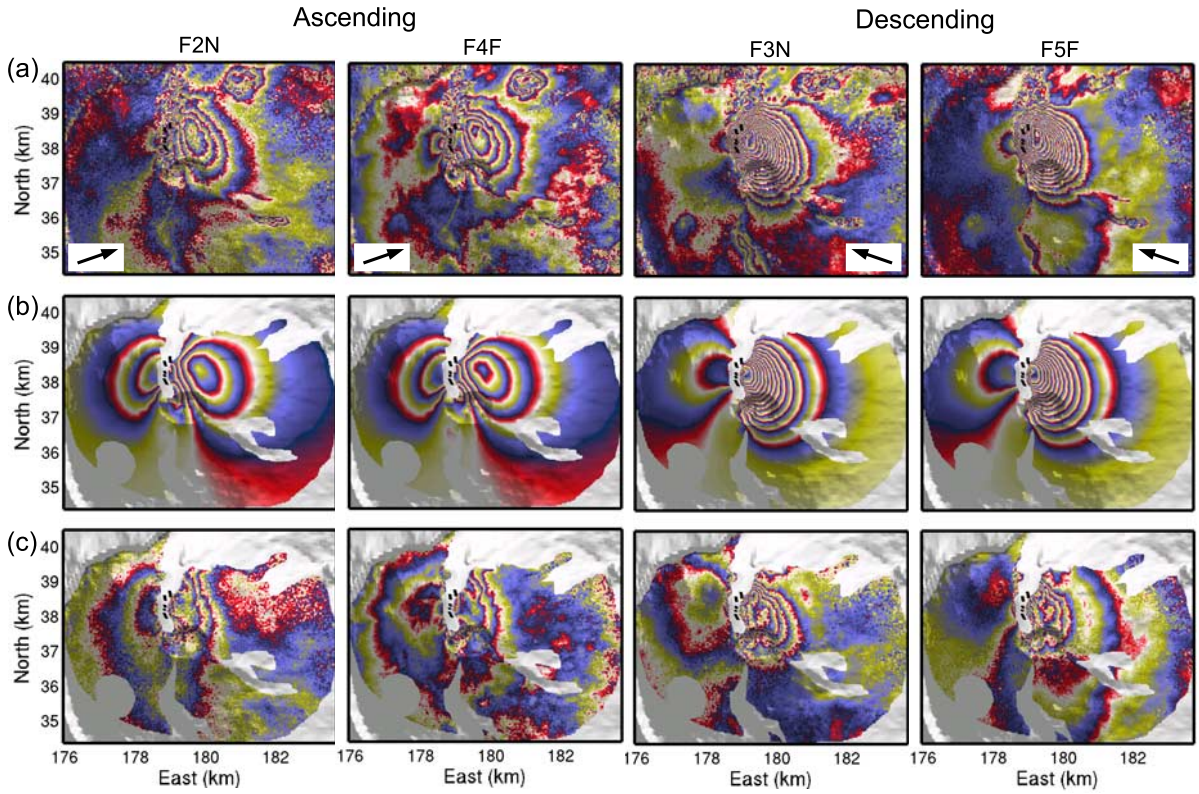

Figure 12. (a) Four interferograms indicating the ground displacements caused by the dike intrusion associated with the February 2000 eruption, superimposed on a DEM. Refer to the caption of Figure 7 for the meanings of gray scale shading and arrows and to Table 3 for data acquisition information. (b) Rewrapped modeled displacements for the four line-of-sight directions corresponding to the maximum PPD model. Recent lava flow areas not used in the misfit evaluation are masked out. (c) Residual displacements between observed and modeled data.